

PAPER • OPEN ACCESS

A systematic printability study of direct ink writing towards high-resolution rapid manufacturing


To cite this article: Qingyang Zheng *et al* 2023 *Int. J. Extrem. Manuf.* **5** 035002

View the [article online](#) for updates and enhancements.

You may also like

- [Simultaneous multi-material embedded printing for 3D heterogeneous structures](#)
Ziqi Gao, Jun Yin, Peng Liu et al.
- [Progresses on cryo-tribology: lubrication mechanisms, detection methods and applications](#)
Wenyan Cui, Hongzhan Chen, Jianxun Zhao et al.
- [Impact of effective volume ratio of a dispersant to silver nano-particles on silicon solar cell efficiency in direct ink-jet metallization](#)
Dong-Youn Shin, Yong-Kee Cha, Han-Hee Ryu et al.

A systematic printability study of direct ink writing towards high-resolution rapid manufacturing

Qingyang Zheng¹, Bin Xie^{1,*}, Zhoulong Xu² and Hao Wu^{1,*} 

¹ Flexible Electronics Research Center, State Key Laboratory of Digital Manufacturing Equipment and Technology, School of Mechanical Science and Engineering, Huazhong University of Science and Technology, Wuhan, Hubei 430074, People's Republic of China

² Guangdong Sygole Intelligent Technology Co., Lt, Dongguan, Guangdong, People's Republic of China

E-mail: binxie@hust.edu.cn and hwu16@hust.edu.cn

Received 28 December 2022, revised 15 February 2023

Accepted for publication 26 April 2023

Published 16 May 2023



Abstract

Direct ink writing (DIW) holds enormous potential in fabricating multiscale and multi-functional architectures by virtue of its wide range of printable materials, simple operation, and ease of rapid prototyping. Although it is well known that ink rheology and processing parameters have a direct impact on the resolution and shape of the printed objects, the underlying mechanisms of these key factors on the printability and quality of DIW technique remain poorly understood. To tackle this issue, we systematically analyzed the printability and quality through extrusion mechanism modeling and experimental validating. Hybrid non-Newtonian fluid inks were first prepared, and their rheological properties were measured. Then, finite element analysis of the whole DIW process was conducted to reveal the flow dynamics of these inks. The obtained optimal process parameters (ink rheology, applied pressure, printing speed, etc) were also validated by experiments where high-resolution ($<100\ \mu\text{m}$) patterns were fabricated rapidly ($>70\ \text{mm s}^{-1}$). Finally, as a process research demonstration, we printed a series of microstructures and circuit systems with hybrid inks and silver inks, showing the suitability of the printable process parameters. This study provides a strong quantitative illustration of the use of DIW for the high-speed preparation of high-resolution, high-precision samples.

Keywords: direct ink writing, extrusion mechanism modelling, computational fluid dynamic (CFD), printability process parameters, high-resolution printing

1. Introduction

Material extrusion-based direct ink writing (DIW) is one of the most versatile additive manufacturing techniques because of its advantages including ink material compatibility [1, 2],

simple operation, and ease of molding [3, 4]. The range of inks used for DIW printing is wide, with the main ink materials including conductive pastes [5–8], hydrogels [9–11], liquid crystal elastomers [12, 13], and shape memory alloys [14, 15]. This wide range of printing materials makes DIW a potential 3D printing method with applications in flexible electronics [16–18], biomedical engineering [19, 20], soft robotics [21, 22], and 4D printing [23].

Figure 1(a) schematically depicts the experimental setup of a standard DIW platform. DIW is an ink extrusion-based additive manufacturing printing method, and the ink is a printable non-Newtonian fluid with organic solvents and additives.

* Authors to whom any correspondence should be addressed.



Original content from this work may be used under the terms of the [Creative Commons Attribution 4.0 licence](https://creativecommons.org/licenses/by/4.0/). Any further distribution of this work must maintain attribution to the author(s) and the title of the work, journal citation and DOI.

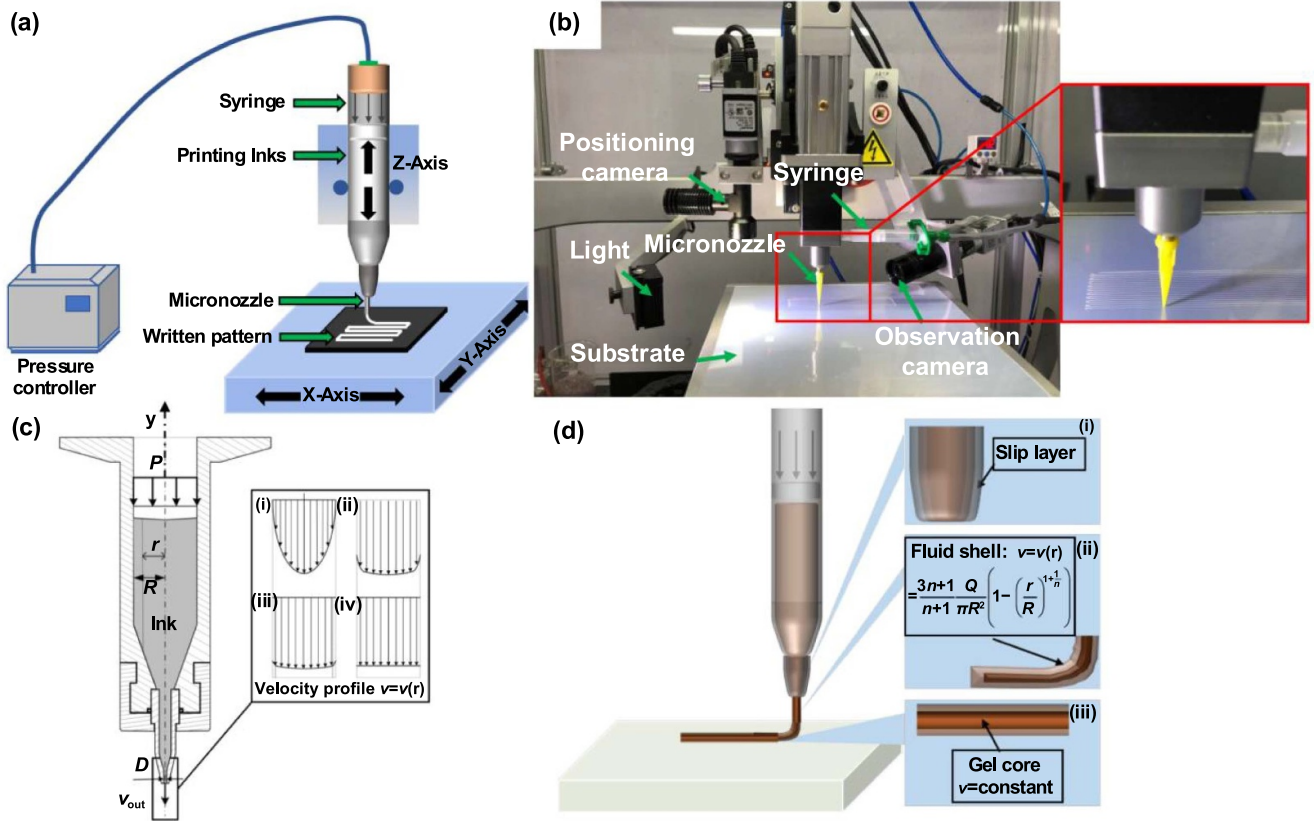


Figure 1. Diagram of DIW print system and dispensing process. (a) Schematic of the extrusion-based 3D printer experimental setup, including print thinned-inks, an extruder (a pressure controller, syringe barrel, and a micro-nozzle), and a three-axis moving platform. (b) Image of self-built DIW experimental platform. (c) Structure view of the syringe and the velocity distribution curve of the different fluid properties. (d) Diagram of the shear thinning process of ink extrusion from a micro-nozzle.

During the DIW pneumatic extrusion process, non-Newtonian fluid is extruded from the micro-nozzle by shear thinning and deposited as a customized pattern under the motion of the print substrate [24, 25]. The accuracy of the printed structure and the effectiveness of extrusion are limited by the characteristics of the ink itself, because low viscosity inks that are suitable for extrusion always result in poor extrusion formability. At the same time, the micro-nozzle extrusion process is subject to shear stress, the flow field directly affects the ink extrusion deposition. During this process, therefore, the quality and property of the printed samples are affected by complex factors. For example, the ink extrusion velocity along the nozzle directly impacts the DIW's efficiency; the uniformity of the extrusion velocity distributions determines the structural integrity of printed objects [26]. In addition, other parameters (ink rheological properties, nozzle diameter, applied pressure) affect the microstructural resolution morphology of the printed samples [27].

Over the past few decades, some pioneer works have been conducted to explore the underlying mechanisms to improve the printability of DIW. For instance, to explore the impact of printing inks, the DIW printable ink quality is evaluated based on the two criteria by using rotational rheology experiment and capillary experiment [28]. The influence of

ink rheological properties on the stretch effect of extruded fibers is studied to print high-resolution fibers [29]. In addition, the flow field characteristics are also essential for DIW, which not only affect the DIW printing efficiency, but also determine the extruded fiber deposition and particle alignment. The particle alignment dynamics are created to analyze the influence of shear stress on particle alignment deposition during DIW printing [30]. The extrusion velocity distribution and the flow state of the ink in the flow channel are investigated to guide the modeling of the extrusion mechanism of the ink [31]. The extruded viscoelastic ink is stretched based on mechanical analysis to print high-resolution fibers; the whole process is achieved by matching the printing speed to the extrusion velocity to stretch the viscoelastic ink [32]. This new strategy is only applicable to inks with a storage modulus large enough to support the stretching effect. However, this research has mostly focused on the influence and printability of single process parameters, and systematic evaluation of the printability of DIW process parameters has rarely been reported. As a consequence, the underlying mechanisms of these key factors on the printability and quality of DIW technique remain poorly understood, which is unfavorable for realizing high-resolution, multi-component, and complex geometries.

Therefore, in this study, to address the aforementioned constraints of DIW technology, we quantitatively and systematically investigated the printability of the DIW technique by the combination of extrusion mechanism modeling, computational fluid dynamics (CFD) finite element simulation, and DIW printing experiment (self-built DIW experimental platform, as shown in figure 1(b)). Non-Newtonian fluid inks with shear thinning characteristics are prepared, and a rotational rheometer tests the rheological properties of the inks to gain insight into the ink characteristics for DIW technology. The effect of process parameters, including ink rheology characteristics, applied pressure, and printing speed on ink extrusion velocity and print filament resolution, is analyzed to deeply understand the high-efficient and high-resolution printable range of DIW technology. Moreover, the influence of extrusion swelling on the print filament diameter during ink extrusion is also discussed to precisely control the resolution of the print filament diameter. By optimizing the printing parameters and obtaining the range of printable process parameters, efficient and stable manufacturing of high-resolution samples can be achieved in preparing DIW printing samples. The applicability of the printable parameters is demonstrated through the manufacture of 2D and 3D demonstrative models and printed circuit systems. The proposed DIW 3D printing process study provides an efficient, simple, and low-cost manufacturing approach for preparing high-resolution, high-precision complex shapes, which may open up new prospects for efficiently manufacturing high-resolution models for practical applications in various fields [33, 34].

2. Materials and methods

2.1. Design and characterization of hybrid ink material

2.1.1. Materials preparation. To research the appropriate range of process parameters, the non-Newtonian fluidic hybrid silicone ink was designed for DIW printing in this study. Six distinct weight ratios of silicone elastomers, SE1700 (Dow Corning), and Sylgard184 (Dow Corning) were combined (10:0, 9:1, 8:2, 7:3, 6:4, and 0:10, where the control subjects were designated 10:0 and 0:10) to form DIW 3D printed viscoelastic ink. More specifically, both SE1700- and Sylgard184-base materials were initially fixed in a 10:1 (base: curing agent) weight ratio and mixed thoroughly using an electronic mixer (GZ120-S, BaoLi, CHN) in a closed 20 ml centrifugal tube. To configure a fully cross-linked ink, SE1700 and Sylgard184 were extensively combined in the electronic mixer at 2000 rpm for 20 min to obtain a fully cross-linked ink mix. Finally, the mixed ink was poured into a 3 cc syringe barrel and then centrifuged at 6000 rpm for 3 min (TG16G, KaiT, CHN) to eliminate air bubbles and form 3D printable viscoelastic ink. The entire ink preparation process was carried out at room temperature. All inks are used within 2 h at room temperature to ensure that the ink viscosity does not change to guarantee the consistency of experimental results.

2.1.2. Measurement of ink rheological characterizations. A hybrid rheometer (Discovery HR-3, DHR) fitted with a parallel plate (diameter = 60 mm) was used to test the rheological parameters of the inks. The gap between the plate and the rotating sensor was fixed at 1 mm. The mixed-ink density ρ was calculated by experimentally measuring the mass and volume of samples. Before measurements, inks were allowed to stand at 25 °C for 5 min. Ink shear viscosity experiments were performed in steady-state flow mode. Measurement of ink viscosity by rheometer rotary test, where the shear rate increases from 0.01 to 1000 s⁻¹. A data point's duration was reduced logarithmically from 30 to 2 s.

Small-amplitude oscillatory frequency sweep mode was used to describe the dynamic viscoelastic characteristics. Measurement of storage and loss modulus of ink by oscillatory stress logarithmic sweep mode, where the shear frequency is 1 Hz, and a shear strain increases from 0.01% to 100%.

To further characterize the thixotropy of inks, viscosity change was measured at different shear strain intervals. Firstly, a steady shear frequency of 1 Hz and a constant shear strain of 0.01 s⁻¹ determined ink viscosity at a period of 0–40 s. Next, ink was measured at a shear strain of 300 s⁻¹ for 15 s. Finally, the recovered viscosity of the ink was measured immediately at 0.01 s⁻¹ shear strain. All rheological experiments were carried out at a temperature of 25 °C.

2.1.3. Hybrid ink constitutive modeling. The interaction between the various components within the ink results in a non-Newtonian system with complex rheological behavior. The rheological properties of this non-Newtonian system directly affect the ink extrusion of the DIW printing system. Therefore, strict control of ink rheology is essential for successful printing of the hybrid ink. If the rheological characteristics of the hybrid ink are known, the shear rate profile of the printing nozzle cross-section can be derived from the shear stress profile. In our analysis, in order to systematically study the hybrid ink extrusion process, a constitutive model is developed to describe the non-Newtonian rheological properties of the hybrid ink. The ink flow state of the DIW printing technology is described using a classical non-Newtonian fluid constitutive model combined with a micro-channel ink extrusion model.

Experimental ink shows a dynamic yield value followed by a shear-thinning behavior. The Herschel–Bulkley constitutive model may be used to characterize the rheological properties of non-Newtonian fluids, which takes the yield stress as an explicit fluid property. Therefore, the flow curve can be analyzed by using the Herschel–Bulkley equation [35]:

$$\tau = \tau_y + k\dot{\gamma}^n, \quad (1)$$

where τ is the ink shear stress in the flow channel, τ_y is the mixed-ink shear yield stress, k is the viscosity coefficient, $\dot{\gamma}$ is the shear rate, and n is the shear thinning index. When $n = 1$, the ink exhibits Newtonian fluid properties and the parabolic velocity profile as illustrated in

figure 1(c, i). When $n < 1$, the ink displays non-Newtonian fluid properties and shear-thinning flow behavior, correspondingly, the velocity distribution characteristics are shown in figure 1(c, ii) ($\tau_y = 0$, power-law fluids) and figure 1(c, iii) ($\tau_y > 0$, yield stress fluids). In addition, the ink flow forms a solid plug flow when there is a large wall slip, no velocity gradient exists in the plug flow area, and the whole ink flows at a constant velocity in every part of the capillary (figure 1(c, iv)) [31]. When $n > 1$, the ink exhibits the shear-thickening property of non-Newtonian fluid. When $\tau < \tau_y$, the ink has zero velocity throughout the runner and no flow occurs.

In the process of extruded ink under pressure, as shown in figure 1(d), the ink is extruded in a solid (gel core)-fluid shell-sliding layer microstructure. The three-zone velocity profile must be considered when considering the rheology of the ink: (1) a thin sliding layer on the inner wall of the nozzle (figure 1(d, i)); (2) surrounded by a yielded (fluid state, velocity $v = v(r)$) shell experiencing laminar flow (figure 1(d, ii)); and (3) a constant-velocity unyielded (gel state) core (figure 1(d, iii)) [4]. High viscosity gel inks are easily extruded from the micro-nozzle and deposited onto the substrate in fine filaments. This implies that the ink viscosity decreases during the shearing process (which is essential for ease of extruding from the micro-nozzle), but recovers when the shearing process is finished (high-viscosity inks help the extruded filaments to form the desired shape on the substrate, i.e. formability). Each of these processes requires accurate control of the rheological characterization.

Compared to inkjet printing, DIW printed samples offer superior formability. More specifically, the distinctive feature of the printed samples is that the extruded fibers quickly recover their high viscosity and remain filamentary. That is, the ink flows at a low viscosity under shear stress (loss modulus $G'' > \text{storage modulus } G'$) but quickly recovers its mechanical properties ($G' > G''$) when the shear stress is removed. The relationship between the G'' and G' directly reflects the shear thinning process and formability of the fibers. Herein, the characteristic parameter $\tan \delta$ is used to describe the loss modulus in relation to the storage modulus:

$$\tan \delta = \frac{G''}{G'}. \tag{2}$$

When $\tan \delta = 1$, ink corresponds to the yield stress point and the solid-liquid critical state. When $\tan \delta < 1$, the shear stress applied to the ink has not reached yield stress, and the ink is in a solid-like initial state. When $\tan \delta > 1$, the τ exceeds the τ_y , and the ink undergoes shear thinning behavior in the liquid-like phase. The classical constitutive model is used to guide the selection of material parameters for the hybrid ink during the finite element analysis. This classical constitutive model provides support for the CFD flow field analysis below.

2.2. Micro-nozzle flow field modeling and finite element simulation

2.2.1. DIW extrusion mechanism modeling.

We utilized the rheological properties of the ink to the non-Newtonian fluid extrusion model to comprehend the extrusion mechanism during the DIW 3D printing procedure, as shown in figure 1(c). The differential equation of fluid motion for the DIW 3D printing extrusion model was established. Then the distribution states of the pressure field, shear stress field, and extrusion velocity field during the printing process were analyzed.

The mass conservation equation, or the continuity equation, is used to describe the fact that the mass of the ink does not change during the printing process. The differential equation of mass conservation is expressed as:

$$\frac{\partial \rho}{\partial t} + \frac{\partial(\rho v_x)}{\partial x} + \frac{\partial(\rho v_y)}{\partial y} + \frac{\partial(\rho v_z)}{\partial z} = 0, \tag{3}$$

where ρ is the fluid density and v is the fluid velocity field. According to the principle of mass conservation, the mass of fluid flowing in per unit time equals to the mass flowing out.

The momentum conservation equation (Navier–Stokes equation) is expressed as:

$$\rho \left(\frac{d\mathbf{u}}{dt} + \mathbf{u} \bullet \nabla \mathbf{u} \right) = \rho \mathbf{g} - \nabla p + \eta \nabla^2 \mathbf{u}, \tag{4}$$

where p is the ink pressure in the flow channel, η is the fluid dynamic viscosity, and $\nabla = \left(\frac{\partial}{\partial x}, \frac{\partial}{\partial y}, \frac{\partial}{\partial z} \right)$ is the Hamilton count. The fluid velocity distribution field can be calculated from the momentum equation.

Neglecting air pressure losses and assuming that the pressure at the barrel inlet equals to the applied pressure. The pressure at different locations along the extrusion element can be calculated by Bernoulli’s energy conservation equation. For viscous fluids, the ink consumes mechanical energy to overcome the viscous resistance in the flow channel. Thus, the Bernoulli equation for a viscous incompressible fluid along a flow line is as follows.

$$\rho g h_1 + \alpha_1 \frac{\rho V_1^2}{2} + P_1 = \rho g h_2 + \alpha_2 \frac{\rho V_2^2}{2} + P_2 + h_w \rho g, \tag{5}$$

where α_1 and α_2 is the kinetic energy correction factor on the cross section, which can usually be approximated as 1; h_w is the flow resistance losses.

$$h_w = \sum h_f + \sum h_j = \sum \lambda \frac{l}{2R_f} \frac{v_f^2}{2g} + \sum \zeta \frac{v_j^2}{2g}, \tag{6}$$

where λ and ζ are both resistance coefficients.

The maximum extrusion velocity v_{\max} at this location can be calculated from the pressure distribution at different locations:

$$v_{\max} = v_y(r=0) = \left(-\frac{dp}{dy} \right) \frac{R^2}{4\eta}. \tag{7}$$

Therefore, the average velocity v_{avg} of different section along the extrusion direction can be calculated by the following equation:

$$\begin{aligned} v_{\text{avg}} &= \frac{1}{A} \int v_y dA = \frac{1}{\pi R^2} \int_0^R v_{\text{max}} \left(1 - \frac{r^2}{R^2}\right) 2\pi r dr \\ &= \frac{v_{\text{max}}}{2} = \left(-\frac{dp}{dy}\right) \frac{R^2}{8\eta}. \end{aligned} \quad (8)$$

For incompressible flow in this study, $\nabla \cdot \mathbf{V} = 0$.

For a fixed control volume, the law of conservation of mass can be expressed in terms of the fact that the masses entering and leaving the control volume in a steady flow must be precisely balanced. Therefore, we have a steady flow:

$$\begin{aligned} \text{Outflow} &= \text{Inflow} \\ \int \frac{\partial \rho}{\partial t} dV + \sum_i (\rho_i A_i V_i)_{\text{out}} - \sum_i (\rho_i A_i V_i)_{\text{in}} &= 0. \end{aligned} \quad (9)$$

Since the incompressible fluid density does not change, the term $\partial \rho / \partial t \approx 0$, so the density integral in equation (9) can be neglected. By simplifying the constant density, the above equation can be simplified as follows:

$$\sum_i (A_i V_i)_{\text{in}} = \sum_i (A_i V_i)_{\text{out}}. \quad (10)$$

or,

$$\sum Q_{\text{in}} = \sum Q_{\text{out}}, \quad (11)$$

where $Q_i = V_i A_i$ is the volume flow.

The average velocity of capillary flow is specified as v_{avg} . The average velocity and cross-sectional area allow the calculation of the volume flow in the flow channel. Therefore, the volume-average velocity can also be calculated as follows:

$$v_{\text{avg}} = \frac{Q}{A} = \frac{1}{A} \int (\mathbf{V} \cdot \mathbf{n}) dA. \quad (12)$$

Combined equation (8) with equation (12), the volume flow Q can be obtained by:

$$\begin{aligned} Q &= \int v_y dA = \int_0^R v_{\text{max}} \left(1 - \frac{r^2}{R^2}\right) 2\pi r dr = \pi R^2 v_{\text{avg}} \\ &= \frac{\pi R^4}{8\eta} \left(-\frac{dp}{dy}\right) = \frac{\pi R^4 \Delta p}{8\eta L}. \end{aligned} \quad (13)$$

where $-\frac{dp}{dy} = \frac{\Delta p}{L}$, and Δp is the pressure drop along the entire length L of the syringe.

The distribution of the shear stress field in capillary flow is an important indicator to judge if the material has reached yield and is ready to flow. The shear stress distribution τ_{wall} can be calculated by the following equation:

$$\tau_{\text{wall}} = \eta \left| \frac{\partial v_y}{\partial r} \right|_{r=R} = \frac{4\eta v_{\text{avg}}}{R} = \frac{R}{2} \left(-\frac{dp}{dy}\right) = \frac{R \Delta p}{2L}, \quad (14)$$

The shear rate distribution $\dot{\gamma}_{\text{wall}}$ of non-Newtonian fluid extrusion flow can be calculated as:

$$\begin{aligned} \dot{\gamma}_{\text{wall}} &= \frac{dV}{dr} = \left(\frac{1}{k}\right)^{\frac{1}{n}} \left[\left(\frac{\tau_{\text{wall}} r}{R} - \tau_y\right)^{\frac{1}{n}} \right] \\ &= \left(\frac{1}{k}\right)^{\frac{1}{n}} \left[\left(\frac{\Delta p r}{2L} - \tau_y\right)^{\frac{1}{n}} \right], \end{aligned} \quad (15)$$

According to the flow field calculation in the above equation, the flow field distribution is only related to the radius of the different cross sections of the circular tube and the inclined syringe nozzle. Therefore, the DIW extrusion modeling applies to both the circular tube and the inclined nozzle models.

2.2.2. CFD simulation analysis of ink flowing in micro-nozzle.

Finite element fluid flow simulations were conducted by ANSYS 2021 R2 CFD, and the extrudate swell study was simulated by ANSYS POLYFLOW. In order to improve the efficiency of the calculation, the following assumptions were proposed to simplify the complex ink flow status.

- (1) An incompressible, highly viscous, non-Newtonian shear thinning fluid model was utilized to simplify the flow behavior of mixed ink materials.
- (2) The mixed ink is evenly filled in the flow channel, and it is isothermal, steady, and laminar in flow during the ink printing process. Reynolds number Re is used to determine the type of ink flow ($Re = \frac{\rho v d}{\mu} = \frac{1196 \times 0.1 \times 0.00021}{10} = 0.0025116 < 2300$, when $Re < 2300$, the pipe flow model is laminar.).
- (3) Considering the high-viscosity inks have a large viscosity force, the inertial and gravitational forces are much less than the viscous forces, and therefore the gravity is neglected.
- (4) For highly viscous flow, a non-slip boundary condition is used, i.e. there is no relative sliding of the ink against the inner wall of the flow channel.

For micro-nozzle flow velocity calculation studies, the wall slip velocity has an effect on the calculation results when the nozzle diameter is very small [36, 37]. Therefore, for small nozzle sizes below $100 \mu\text{m}$, the effect of wall slip on flow rate prediction should be considered [38]. The density ρ , and the yield shear stress τ_y were obtained by experiment. The shear thinning index n , and the viscosity coefficient k were obtained by fitting the experimental data with the Herschel-Bulkley model.

2.3. DIW printing experiment

2.3.1. DIW printing of viscoelastic ink.

Self-designed DIW 3D printer experimental platform based on air pressure-driven extrusion. The DIW experimental platform is constructed with three main components: (i) a pressure controller, (ii) pneumatically driven extrusion components, (iii) and an X-Y-Z three-axis moving stages. The pressure controller provides the extrusion force of inks, and the extrusion velocity of inks is

controlled by the applied pressure and the characteristics of the inks. The printed samples were drawn using the structural design software AutoCAD and converted into G-code for reading by the control. The pressure control system drives the air pump for the regulation of the applied pressure. The configured inks were deposited onto the substrate by extrusion through nozzles of different diameters. Nozzles with different structures and diameters used in the experiments were purchased commercially.

2.3.2. Measurement of printing extrusion velocity and printed filaments diameter. The weighing method is used to measure the weight of extruded ink within 30 s, and then calculate the extrusion flow rate and average extrusion velocity. The fiber structure of extruded inks was observed by an optical observation camera (acA1920-50gm, Basler, SGP), and the diameter of printed filaments was measured using an optical microscope (acA2500-14gm, Basler, SGP).

3. Material characterization and CFD results

3.1. Rheological behavior of the hybrid ink

Ink rheological characteristics are an essential indicator of the printability of DIW 3D printing technology [39]. The inks used for DIW 3D printing should meet two requirements: shear-thinning properties and self-healing formability. More specifically, shear thinning behavior means that the ink has a sufficiently low shear viscosity at high shear stress to ensure that the ink is steadily extruded from the micro-nozzle without clogging. On the other hand, self-healing formability means that the printed fibers have a high strength and storage modulus to ensure that the printed pattern retains its original shape.

Static rheology tests are used to characterize the viscosity properties of inks, and to reflect the viscosity variation law and shear-thinning behavior [40]. Some pioneer works have been conducted to explore particular ink systems to optimize inks for various applications [41, 42]. This paper uses this proven ink formulation to investigate the effect of ink characteristics on the quality of printed samples during the DIW printing process. Figure 2(a) indicates the shear rate effect on the viscosity of various PDMS hybrid inks. Hybrid ink viscosity decreases logarithmically with increasing shear rate, and the viscosity of pure Sylgard184 is constant and barely varies with the shear rate. The ink has an initial high viscosity of 10^5 Pa·s at the low shear rate (10^{-2} s $^{-1}$), and the shear viscosity has dropped to 5 Pa·s at the high shear rate (10^3 s $^{-1}$). The above phenomenon clearly demonstrates the shear thinning behavior of the hybrid inks. Figure 2(b) shows the variation of shear stress with the shear rate of the prepared inks. The shear stress of pure Sylgard184 ink is linearly related to the shear rate (i.e. Newtonian fluid). The constitutive model of equation (1) can be obtained for the formulated ink by fitting the experimental shear stress to shear strain relationship. The experimental data and the fitted curves are shown in figure 2(c), and the figure shows that the Herschel–Bulkley constitutive model can excellently characterize the rheological properties of the hybrid inks. The

specific parameters of the fitted general for each formulated ink are shown in table 1.

The self-healing formability of the ink can be characterized by dynamic rheology, which studies the oscillatory shear characteristics of fluids subjected to periodic stresses by applying periodic effects to the material [43]. Figure 2(d) shows the storage (G') and loss (G'') modulus of various hybrid inks in relation to shear stress. The G' of the hybrid ink is much bigger than G'' before reaching the shear yield stress, which shows that the hybrid inks for printing exhibit a stable solid-like phase. When the shear stress is greater than the shear yield stress, the G' and G'' sharply decrease and G' is less than G'' , which means that the hybrid inks exhibit a flowable liquid-like phase. The storage modulus G' increase with increasing SE1700 content in the hybrid ink, and the G' and G'' for Newtonian fluid pure Sylgard184 ink are constant. Figure 2(e) shows the characteristic parameter $\tan\delta$ (equation (2)) as a function of shear stress. Section 2.1 shows that $\tan\delta = 1$ is the critical point of solid–liquid transition, and the intersection with each ink corresponds to the shear yield stress τ_y of the hybrid ink. The top half shows the liquid-like phase after the shear shinning of the hybrid ink, and the bottom half shows the unyielding solid-like phase. When the shear stress exceeds the yield stress, the ink changes from a solid-like phase to a liquid-like phase, facilitating the flow of ink from the micro-nozzle. The shear yield stress τ_y (65.12, 154.70, 232.48, 592.68, and 719.23 Pa) increases with increasing SE1700 content in the hybrid ink.

To further characterize the thixotropy of hybrid inks, figure 2(f) has described the dependence of hybrid ink viscosity on time at various shear rates. The thixotropic ink behaviors of the DIW 3D printing process have three stages, including the initial shear rate (0.01 s $^{-1}$) during the ink store segment, the shear rate (300 s $^{-1}$) as the ink extrusion from the nozzle, and the minimum shear rate (0.01 s $^{-1}$) after the ink has been extruded. At the first phase of the thixotropic experiment, the initial viscosity of the solid-like ink was measured at 10^4 Pa·s. In the second stage, when the ink is extruded from the nozzle, the shear viscosity drops significantly to 10 Pa·s when the shear rate suddenly increases to 300 s $^{-1}$. Subsequently, the hybrid ink recovery viscosity of 10^4 Pa·s when the ink is extruded, and the shear rate falls back to 0.01 s $^{-1}$. Because hybrid ink can maintain high viscosity under low shear stress, it has improved storage and shape retention capabilities. While the extremely low hybrid ink viscosity under high shear stress promotes smooth ink extrusion during printing. The hybrid inks exhibit excellent shear thinning and viscosity recovery properties that are suitable for high-resolution sample preparation using DIW 3D printing technology.

3.2. Flow field distribution in the DIW 3D printing extrusion process

The ink flow field distribution of DIW printing technology directly reflects the flow condition of the printing ink and has a significant impact on the shape and quality of the printed sample. As a result, to examine the effect of process parameters on the quality of printed samples more objectively, we

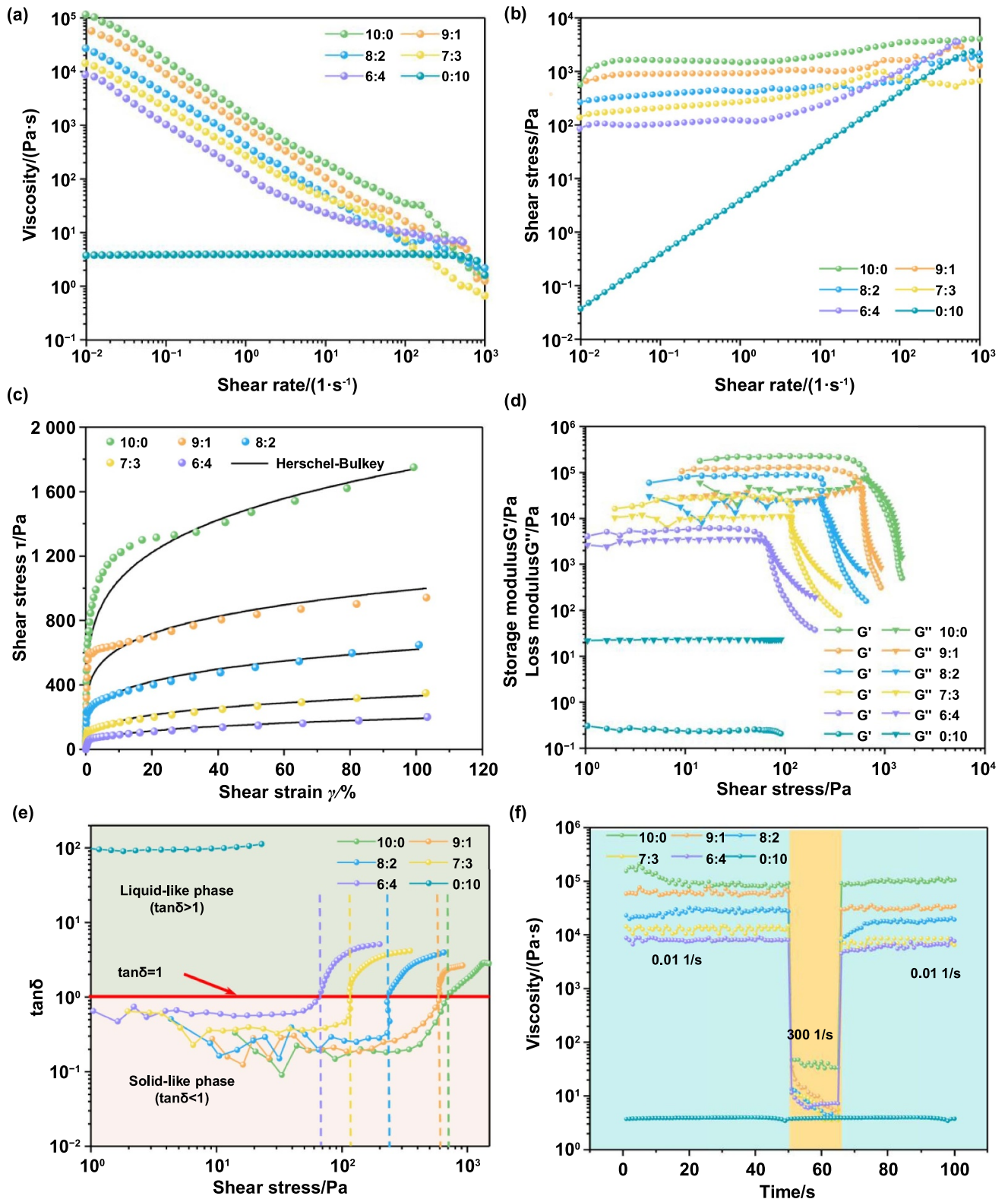


Figure 2. Rheological properties analysis of PDMS resin inks 10:0, 9:1, 8:2, 7:3, 6:4, and 0:10. (Where the inks Ink10:0 and Ink0:10 were used as control groups). (a) The shear rate effect on the viscosity of various PDMS resin inks. (b) Variation of shear stress with the shear rate. (c) Experimental results for shear stress vs. shear strain, and the Herschel-Bulky constitutive model were obtained by fitting the experimental data. Detailed data of the constitutive model are shown in table 1. (d) Storage (G') and loss (G'') modulus of PDMS resin inks in relation to shear stress. The hybrid ink yield stress points at the intersection of storage modulus and loss modulus. (e) Variation of characteristic parameters $\tan \delta$ with the shear stress in oscillatory shear experiments. (f) Viscosity characteristics with time in thixotropic experiment, where the shear rate is abruptly increased from 0.01 s^{-1} to 300 s^{-1} at 50 s and returned to 0.01 s^{-1} at 65 s.

Table 1. Fitting Herschel–Bulkley constitutive model coefficients from experimental data.

Mixed inks	Yield stress τ_y (Pa)	Viscosity coefficient k (Pa·s)	Shear-thinning Index n	Correlation coefficient R^2
10:0	719.23 ± 71.82	630.82 ± 64.01	0.202 ± 0.066	0.95649
9:1	592.68 ± 44.88	391.70 ± 41.23	0.220 ± 0.052	0.96685
8:2	232.48 ± 37.54	204.56 ± 22.46	0.240 ± 0.037	0.99782
7:3	154.70 ± 14.14	92.86 ± 16.07	0.276 ± 0.032	0.99778
6:4	65.12 ± 5.65	43.26 ± 6.42	0.324 ± 0.030	0.99893

explored the influence of flow field distribution on the quality of printed samples at various process parameters. Figure 3(a) depicts the pressure distribution along the flow channel as calculated by the finite element method with a 300 kPa inlet pressure. Figure 3(b) indicates the detailed static pressure distribution curve along the flow channel axis under different applied inlet pressures. The pressure remains consistent with the applied inlet pressure value during the ink store segment, and then drops sharply to 0 kPa in the shear section of the flow channel. The considerable pressure drop in the flow channel results in a significant increase in the ink shear force, which directly increases the extrusion velocity of the hybrid ink.

Generally, velocity and shear stress distribution fields are essential factors affecting DIW printing. Studying axial (Y -axis) velocity distribution is vital for DIW high-speed printing. The velocity distribution field, as shown in figure 3(c), depicts the velocity of ink extrusion from the micro-nozzle, which directly affects DIW printing efficiency. The ink extrusion velocity in the syringe barrel is quite low, and no significant change in the velocity gradient. However, there is a considerable gradient increase in velocity at the nozzle outlet. Figure 3(d) indicates the radial section velocity profile at various distances from the nozzle (0, 0.5, 1, 2, and 8 mm from the outlet). It is found that the velocity at the flow channel's central axis is substantially larger than at the flow channel's edges in the same horizontal section. The ink velocity on the central axis increases significantly with the narrowing of the flow channel in the extrusion direction. The study found that the velocity distribution curve of the non-Newtonian fluid shows a nonlinear gradient change, which is consistent with the results of the velocity field analysis in section 2.2.

As illustrated in figure 3(e), the local shear stress is highest near the flow channel wall, and the nozzle's local shear stress is higher than that of the syringe barrel. The local shear stress in the central axis remains constant. Then the local shear stress increases continuously in the extrusion direction and reaches the maximum at the nozzle outlet. Figure 3(f) shows the detailed wall shear stress distribution curve along the nozzle axis under different applied inlet pressures. From the velocity field distribution (figure 3(c)), it is found that the larger wall shear stress corresponds to faster changes in ink extrusion velocity. The ink extrusion velocity is positively correlated with the wall shear stress. According to the shear thinning characteristics of hybrid ink, the larger the local

wall shear stress, the lower the viscosity of the material. The lower viscosity ink facilitates the extrusion from the micro-nozzle and enables the high-precision forming of the fine filaments.

The pressure drop causes a tendency for the ink to flow from high to low pressure. When the maximum shear stress applied to the ink within the flow channel is less than the yield stress of the hybrid ink, a plug flow zone occurs, which is the unyielding zone that results in constant velocity. If there is a wall shear stress $\tau_{\text{wall}} > \tau_y$ at a certain radius, Poiseuille flow [44] is generated; otherwise, it will not flow. According to the above simulation analysis, the pressure field and shear stress distribution directly affect the ink extrusion state. Therefore, the micro-nozzle flow field distribution analysis through the CFD method is of great significance for further study of the DIW 3D printing process.

3.3. Finite element simulation reliability verification

The reliability of the proposed extrusion mechanism model and CFD simulation results were verified by comparing the simulation and experimental results of different inks. Figure 4(a) depicts the distribution of the various ink pressure fields calculated using the TT160 nozzle. The pressure field drops sharply to 0 through the transition section of the flow channel. The distribution of the different ink shear stress fields along the flow channel is illustrated in figure 4(b). Higher shear stress at the outlet facilitates ink extrusion from the micro-nozzle. Due to the high viscosity ink storage modulus and shear yield stress being larger, the wall shear stress of high viscosity ink is larger.

The simulation and experimental results of the ink extrusion velocity are shown in figure 4(c). It can be found that the extrusion velocity increases with the applied pressure, and the extrusion velocity of high viscosity ink is smaller due to the higher shear yield stress. Figure 4(c) shows that the experimental results agree well with the simulated results at low pressures, while at high pressures, the experimental results are smaller than the simulated results due to the elevated channel resistance (channel resistance h_w increases with increasing velocity). The DIW device nozzle connection errors lead to fluctuations in experimental results. Overall, our proposed extrusion mechanism modeling and CFD flow field simulation method can effectively evaluate the DIW extrusion process, and the simulation results can provide guidance for optimizing printable parameters.

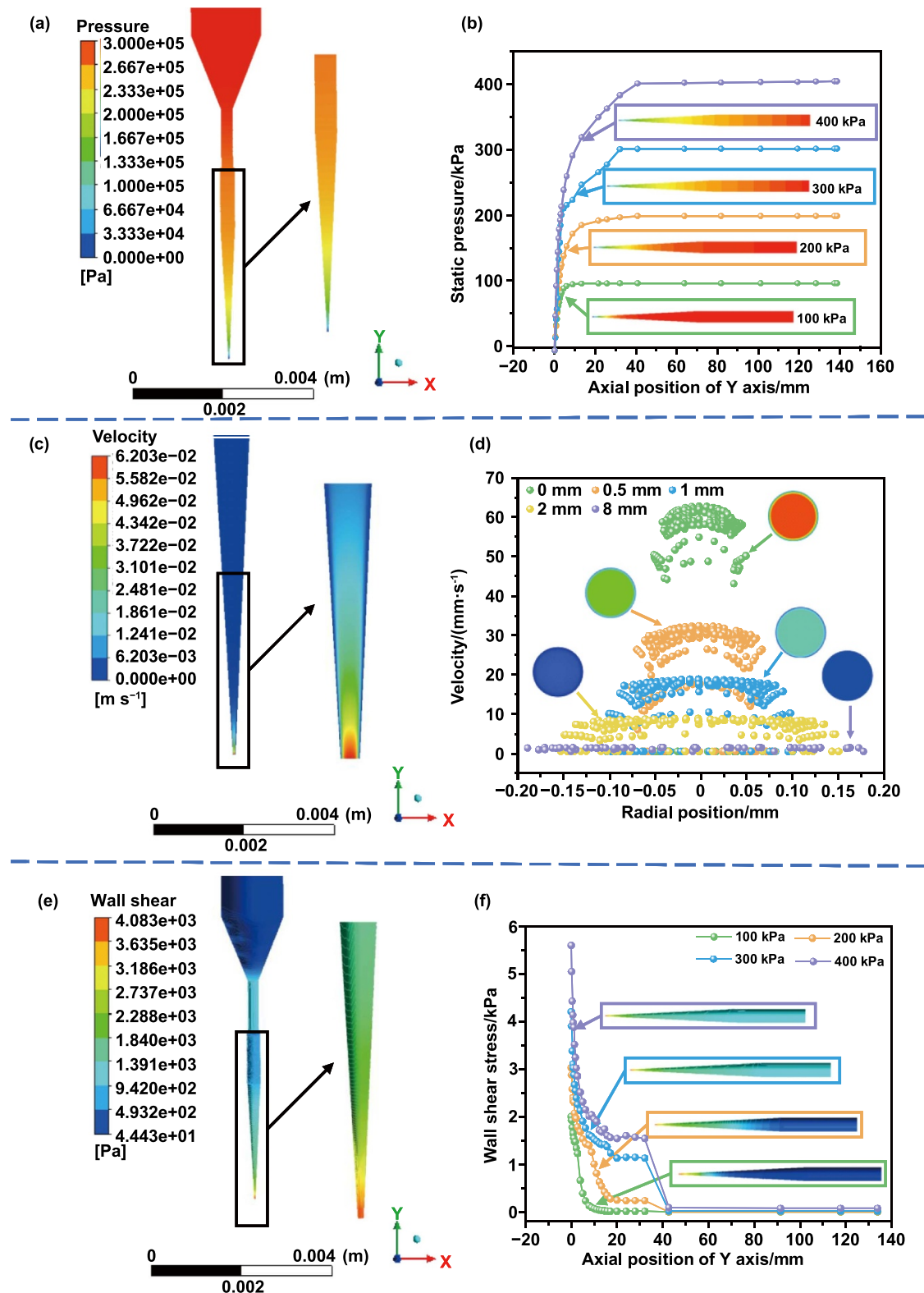


Figure 3. CFD flow field results of the tapered tips nozzle (TT nozzle) along the nozzle channel. The diameter of the TT nozzle is 160 μm, and the hybrid PDMS resin ink is Ink8:2. (a) Pressure distribution in the flow channel. (b) The static pressure distribution diagram of the simulated fluid flow along the channel in the same TT nozzle with the various applied inlet pressure. (c) Velocity distribution in the flow channel. (d) Velocity images at different sections in the flow channel. (The legend shows the distance from the tip of the nozzle along the y-axis, and the circular velocity cloud diagram indicates the radius direction cross-section, and the arrows correspond to the legend position speed). (e) Wall shear rate distribution in the flow channel. (f) The wall shear stress distribution diagram of the simulated fluid flow from CFD analysis along the channel in the same TT nozzle with the various applied inlet pressure.

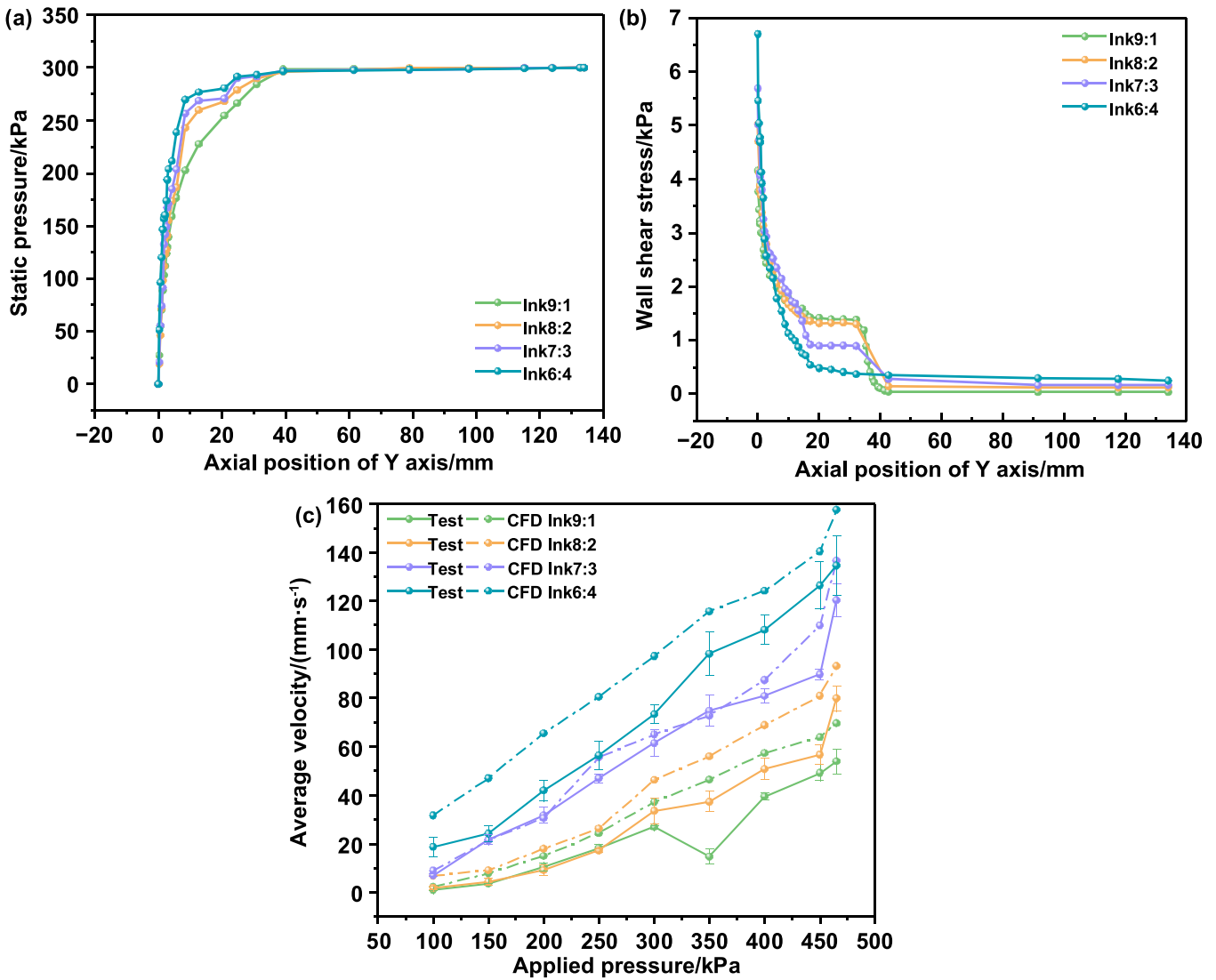


Figure 4. CFD simulation results verification (using TT160 nozzles, the diameter of tapered tips nozzle is 160 μm). (a) The static pressure distribution of the simulated fluid flow along the flow channel at different inks (Ink9:1, Ink8:2, Ink7:3, and Ink6:4). (b) The wall shear stress distribution diagram of the simulated fluid flow from CFD analysis along the channel (applied pressure 300 kPa). (c) The extrusion velocity comparison diagram under various PDMS resin inks.

4. Experimental results

4.1. Process tests and simulation analysis of extrusion velocity

The mass of extruded ink was measured under different experimental conditions according to the weighing method. By altering the value of applied pressure, material viscosity, and micro-nozzle diameter, the mass of the extruded ink was measured for 30 s in different process parameters. Variations of ink density can be ignored based on the assumption that the ink is incompressible. Therefore, the average velocity of extruded ink can be calculated by the following equation,

$$v_{\text{average}} = \frac{m}{\rho t A}, \quad (16)$$

where v_{average} is the extruded average velocity, m is the mass of material extruded from the nozzle, ρ is the density of printed material, t is the extruded time of the mass m , and A is the nozzle outlet's cross-sectional area.

The influence of micro-nozzle structure on the DIW 3D printing extrusion velocity is depicted in figures 5(a)–(c). The axial (Y axis) wall shear stress field indicates that the shear stress of the inclined nozzle (TT110, TT160, and TT210) is much greater than that of the straight nozzle (ST160 and ST260) under the same applied pressure (figure 5(a)). The simulation (figure 5(b)) and experimental (figure 5(c)) results of the average extrusion velocity show that the micro-nozzle with high shear stress field corresponds to a larger extrusion velocity. The diameter of the micro nozzle directly affects the extrusion velocity, the average extrusion velocity increases as the micro-nozzle diameter grows. The ink is easily extruded

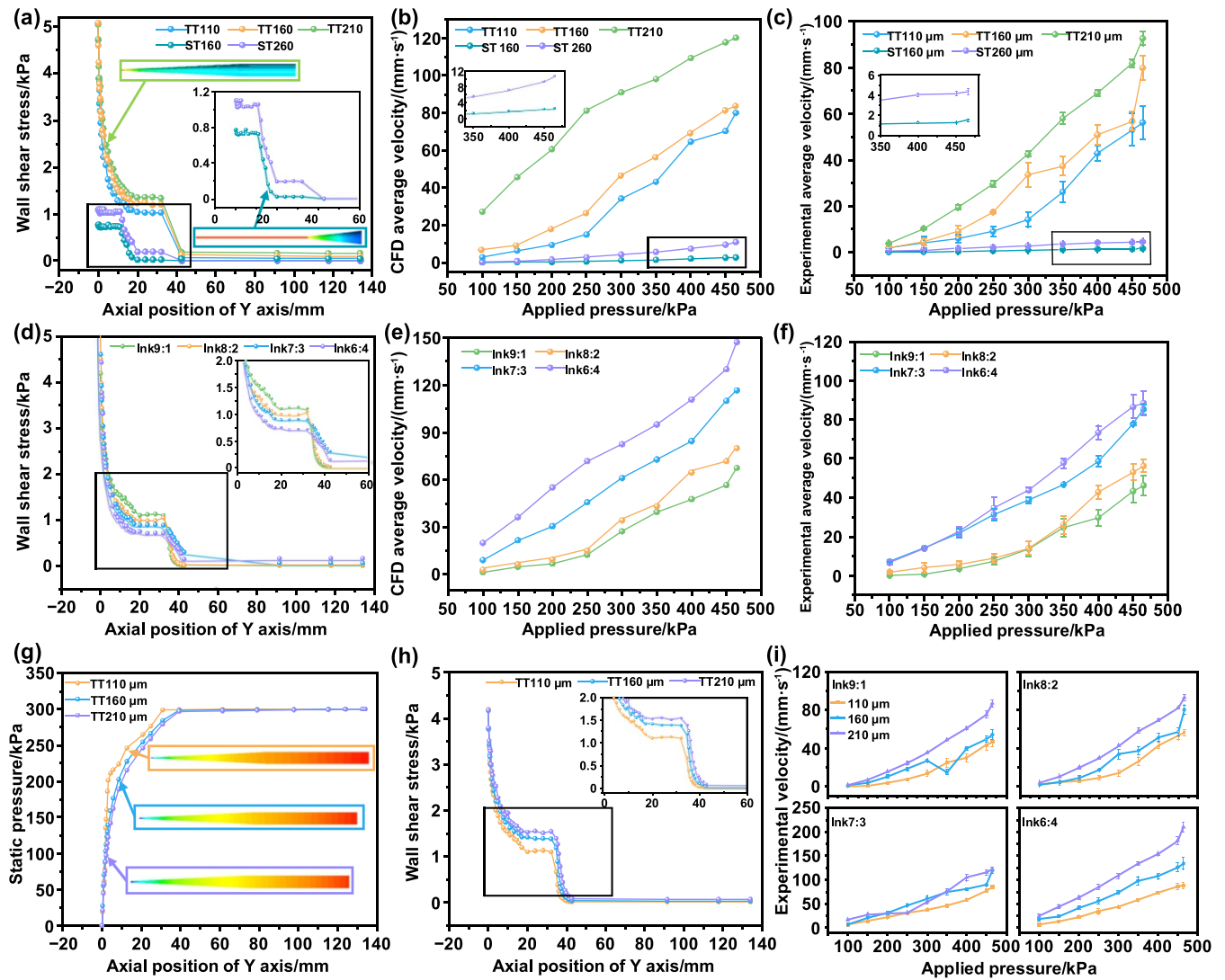


Figure 5. The results of CFD simulation and experimental results under different printing process parameters. (a) The wall shear stress distribution diagram of the simulated fluid flow from CFD analysis along the channel (applied pressure 300 kPa, micro-nozzle TT110, the diameter of tapered tips nozzle is 110 μm . ST160, the diameter of the straight nozzle is 160 μm). (b) The nozzle outlet average velocity vs. applied inlet pressure from the CFD simulated fluid flow in the flow field, and (c) the DIW experimental results under the various nozzle type. (d) The wall shear stress distribution diagram of the simulated fluid flow from CFD analysis along the channel (applied pressure 300 kPa, micro-nozzle TT110). (e) The nozzle outlet average velocity vs. applied inlet pressure from the CFD simulated fluid flow in the flow field, and (f) the DIW experimental results under the various PDMS resin inks 9:1, 8:2, 7:3, and 6:4. (g) The static pressure distribution diagram, and (h) the wall shear stress distribution diagram in the flow channel (applied pressure 300 kPa, ink Ink9:1). (i) The nozzle outlet average velocity vs. applied inlet pressure from the DIW experimental results under the various PDMS resin inks and the nozzle types.

and does not clog the micro-nozzle due to the steady lowering of the inner diameter of the tilted nozzle. The inclined nozzle requires only a small amount of applied pressure to ensure the high-precision forming of DIW printing. Therefore, we take the inclined nozzle as the main research object in the subsequent research. Figures 5(d)–(f) illustrate the influence of ink rheological properties on the DIW printing extrusion velocity. Because the shear yield stress of high viscosity ink is large, high viscosity inks require higher shear stress, and the extrusion velocity is smaller.

Figures 5(g) and (h) illustrate the pressure and wall shear stress fields for the three nozzles. The pressure field demonstrates that the smaller diameter nozzle has a larger high-pressure area, but the wall shear stress is lower. Figure 5(i) shows the experimental results of extrusion velocity with different nozzles by using various prepared hybrid inks. There is a crossover between the extrusion velocity of different nozzles, which may be attributed to the connection error between the nozzle and the channel, and the machining error of the nozzle itself. The extrusion velocity distribution provides guidance

for studying the optimization of DIW 3D printing process parameters.

4.2. Analysis of extrudate swell and adjustment of swelling ratio

Extrusion swelling phenomenon (i.e. Barus Effect) demonstrates that when non-Newtonian fluid is extruded from small holes, capillaries, or slits, the diameter of the extruded material at the outlet is usually larger than the diameter of the flow path. The extrusion swelling is a common phenomenon in the extrusion of non-Newtonian fluids. In most theoretical models, it is assumed that the diameter of the extruded fiber is considered to be identical to the inner diameter of the micro-nozzle. However, the influence of extrusion swelling reduces the precision of the printed model significantly during the actual printing process. Therefore, the influence of the extrusion swelling on the precision of the extruded fibers must be considered. For the DIW printing extrusion process, the accurate prediction of the extruded fiber diameter directly determines the model's accuracy and the printed sample's quality. In this study, the swelling ratio is introduced to quantify the impact of extrusion swelling on the DIW 3D printing process. The swelling ratio B quantifies the extruded swelling phenomena, which is defined as the ratio of extruded fiber diameter $D_{\text{extrudate}}$ to nozzle diameter D_{nozzle} following extrusion stabilization [45].

$$B = \frac{D_{\text{extrudate}}}{D_{\text{nozzle}}}, \quad (17)$$

where $D_{\text{extrudate}}$ is the diameter of printed filament, and D_{nozzle} is the inner diameter of micro-nozzle.

Based on the original CFD simulation model, the hybrid ink extrusion process simulation from the micro-nozzle has been conducted. As shown in figure 6(a), the fibers extruded from different micro-nozzles all exhibit the swelling phenomenon of increasing diameter. As a result, when the fibers exit the nozzle, the diameter swelling ratio increases rapidly at first, then gradually increases to a constant value after 5 mm from the nozzle outlet. Figure 6(b) depicts the evolution of fiber diameter swelling at various micro-nozzle sizes. In a subsequent study, the nozzle extrusion swelling ratio is obtained by measuring the experimental extruded fiber diameter.

Figure 6(c) compares the variation of extruded fiber swelling ratio with inlet applied pressure for different micro-nozzle. The swelling ratio can increase rapidly with applied pressure and gradually stabilize. The increased applied pressure leads to increased ink extrusion velocity, which shortens ink residence time in the flow channel. Therefore, the elastic storage energy of the ink extrusion is not fully released in the shear section, resulting in an increasing ratio of extrusion swelling. As micro-nozzle diameter increases, the extrusion swelling ratio decreases. Figure 5(g) shows that the high-pressure area has a greater impact with the small nozzle configuration. The elastic storage energy of the ink in the high-pressure area increases, resulting in an increasing ratio of extrusion swell. Figure 6(d) indicates the experimental results with different micro-nozzle. The experimental results of the swelling

ratio are slightly greater than the simulated results because of the ink surface tension in actual operation. The swelling ratio firstly increases quickly until the applied pressure of 400 kPa, and then decreases slowly. This is because the effect of gravity is more pronounced with the extrusion pressure in the test. Figures 6(e) and (f) show the simulation and experimental results for the variation of extruded fiber swelling ratio with the applied pressure under different ink formulations. It is found that as ink viscosity increased, the swelling ratio dropped. Besides, gravity affects the extrusion swelling ratio of the experimental results during high-speed extrusion.

4.3. Printability process tests of viscoelastic inks

Printing performance and fiber accuracy in the DIW 3D printing method is primarily governed by process factors such as ink rheological characteristics, applied inlet pressure, and printing speed. When the ink formulation is selected, the resolution of the printed filament can be adjusted by varying the applied pressure and substrate move speed. This study investigated various applied pressure and printing speed ranges to optimize the printing process parameters for the four inks and the different micro-nozzles. Figure 7(a) depicts the fluctuation in trace width of printed fiber lines with respect to various DIW printing speeds. The applied pressure is set as 300 kPa, and the Ink8:2 is used for printing. Under the micro-nozzle diameter of 210 μm , ink accumulation occurs at printing speeds range of 1–30 mm s^{-1} , resulting in the width of printing fiber (>300 μm) being much larger than the micro-nozzle diameter. The width of the printed fibers becomes narrower as the printing speed increases in the range of 30–80 mm s^{-1} . This is because the printing speed does not match the extrusion velocity, making it difficult for the extruded hybrid inks to be deposited simultaneously, so the lines are stretched and gradually thinner. If the printing speed surpasses 80 mm s^{-1} , the fiber lines appear discontinuous or even broken. This is because the printing speed has exceeded the critical printable speed, resulting in discontinuous printing lines that severely affect the quality of printed samples. Different print nozzles correspond to the printable range. Figure 7(b) depicts the trace width and morphology of 2D planar fibers printed under different micro-nozzle diameters. The printing applied pressure is set as 300 kPa, and the printing speed of 30 mm s^{-1} is used to print Ink8:2 prepared ink.

The applied pressure is another process parameter affecting the printed fibers' accuracy. The applied pressure mainly affects the extrusion velocity of ink, and then affects the volume of ink extruded per unit time. Figure 7(c) shows the variation of the printed line width with applied pressure at different printing speeds (10, 20, and 30 mm s^{-1}). The micro-nozzle with a diameter of 110 μm is selected for DIW printing. And it turns out that as the applied pressure increases, the volume of ink extruded in the same amount of time also increases, resulting in an increase in the line width. When the applied pressure is less than 100 kPa and the printing speed is 10 mm s^{-1} , discontinuous printing can occur due to insufficient applied pressure. This is because the applied pressure

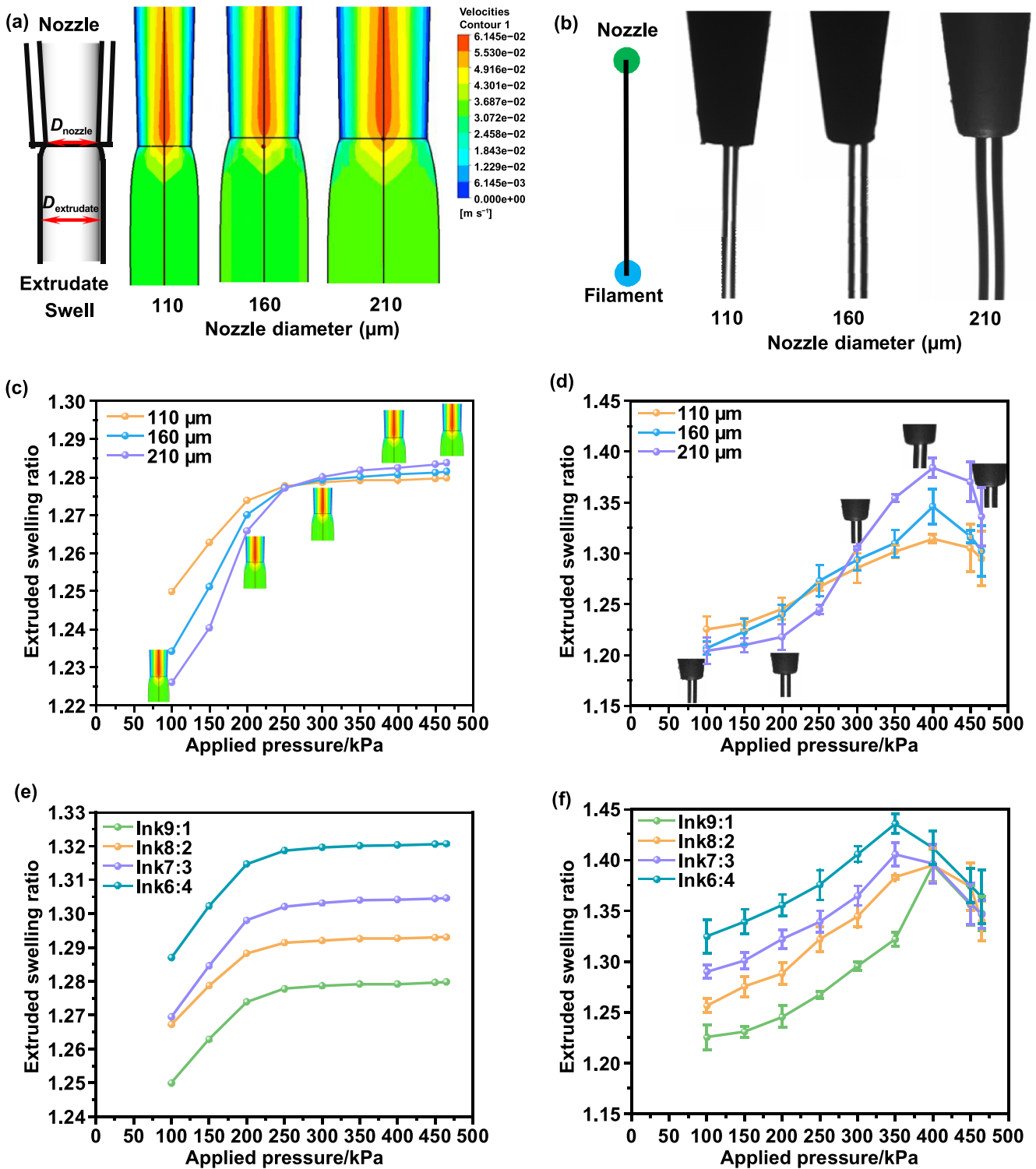


Figure 6. The FEM simulation results and experimental results of extrudate swell characteristics under different printing process parameters. (a) FEM simulation diagram ((b), experimental microscope images) of inks extrusion swell in the same inlet pressure of 300 kPa using Ink9:1. (c) FEM simulation diagram ((d), experimental results) and a folded line graph of inks extruded swelling ratio at different applied inlet pressure. (e) FEM simulation results ((f), experimental results) of extruded swelling ratio vs. applied inlet pressure under the various PDMS resin inks.

does not provide a sufficiently stable working pressure drop, which makes it difficult for the printed fibers to be deposited consistently on the substrate. When the applied pressure

exceeds 400 kPa, the printing speed of 10 mm s^{-1} is too low, causing ink accumulation on the print line. Figure 7(d) shows the 2D fibers with excellent print sample quality.

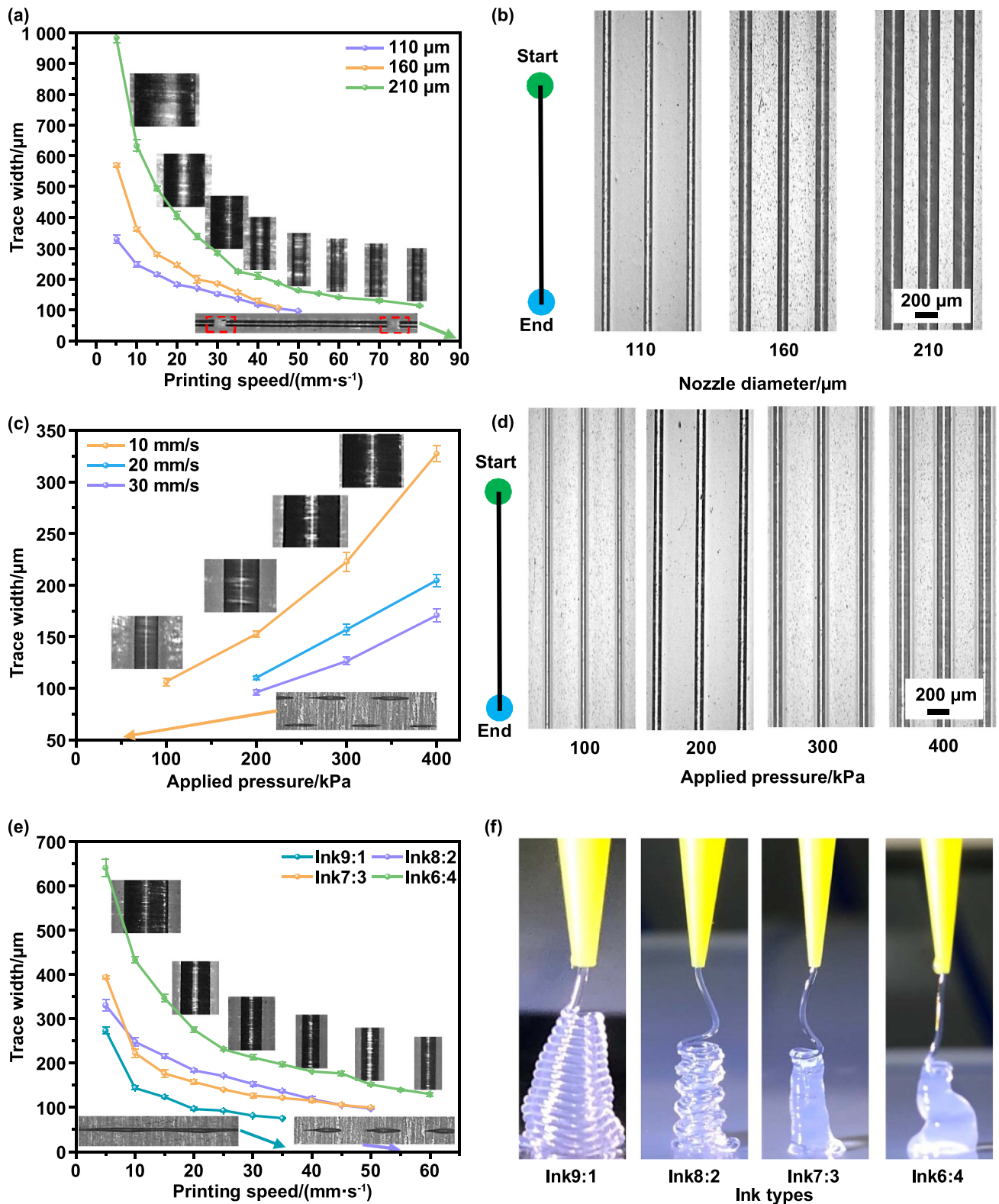


Figure 7. Wire trace characteristics under various process parameters. (a) Printed fiber trace width at various printing speeds. (b) Microscope images of printed lines for Ink8:2 in the same inlet pressure of 300 kPa under 30 mm s⁻¹. (c) Printed fiber trace width under varied applied pressures. (d) Microscope images of printed lines for Ink8:2 in the same print speed of 20 mm s⁻¹ by using TT110. (e) Printed fiber trace width with varying ink rheological properties. (f) Printed diagram of the various PDMS resin inks 9:1, 8:2, 7:3, and 6:4 based on the TT210 nozzle.

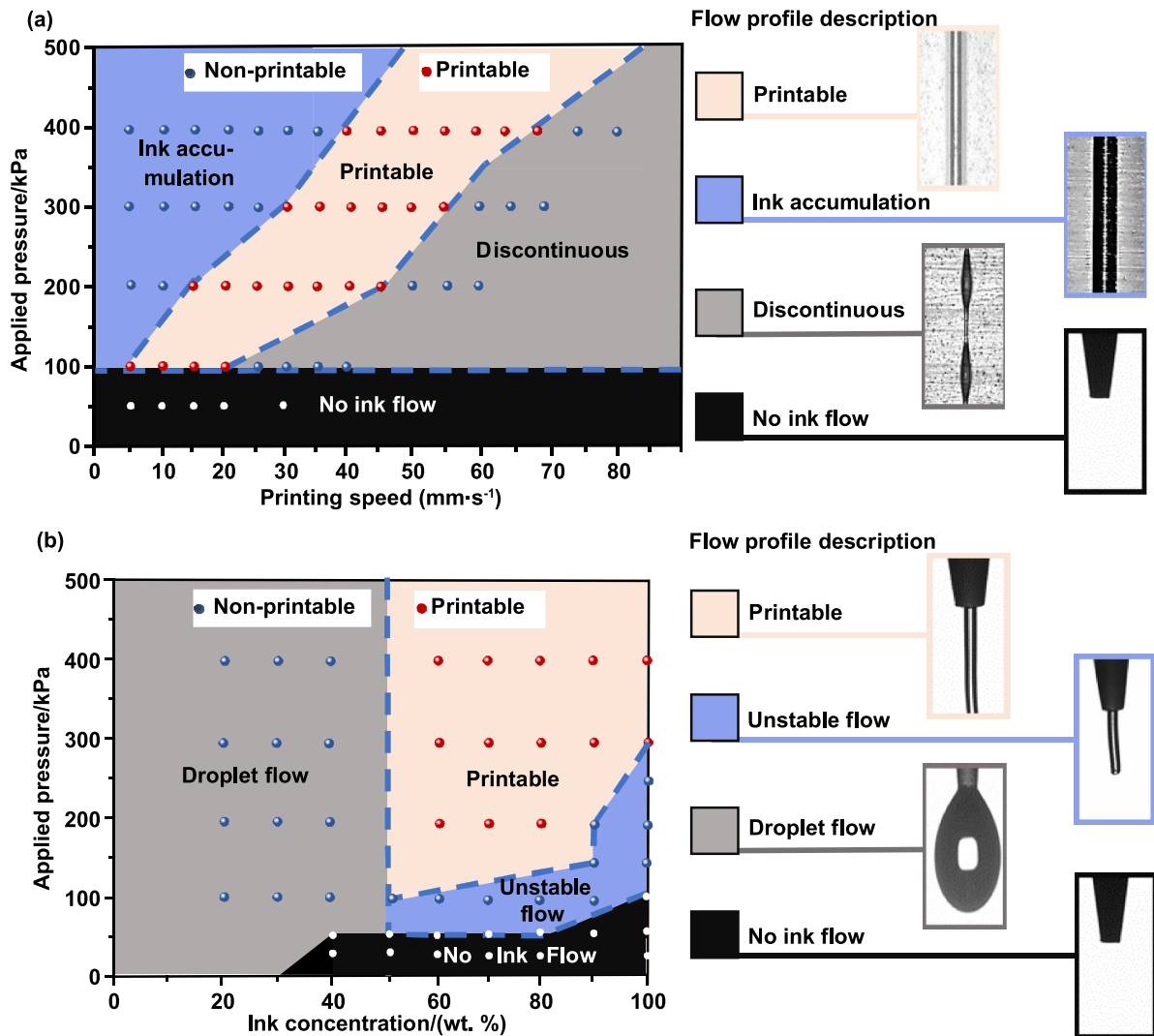


Figure 8. DIW 3D printing phase diagram of PDMS resin inks solution at 25 °C. (a) Experimental data was plotted in the phase image under different applied inlet pressure and printing speed. (b) Empirical data was plotted in the phase image under different applied inlet pressure and the various PDMS resin ink (SE1700 weight/total weight). Dots represent experimental data (the red dot is the printable parameters, the white dot is the no ink flow, and the blue dot parameters cannot print a controlled pattern). The dotted line and block area represent the theoretical prediction.

Figure 7(e) shows the variation of the printed line width with printing speed at different ink formulations. The printing applied pressure is set as 300 kPa, and the micro-nozzle with a diameter of 110 μm is used to print. The volume of ink extruded per unit time increases as the ink viscosity decreases at the same applied pressure. Therefore, low viscosity inks print wider lines under the same conditions. The width of printed fibers decreases as the printing speed increases, and then discontinuous print lines when printing speed exceeds the printable critical speed. Figure 7(f) shows the morphology of extruded fibers printed with each ink formulation at the same micro-nozzle (210 μm). It can be seen from section 3.1 that the Ink9:1 prepared ink has high modulus and recovery viscosity, which facilitates the self-healing formability of the printed structures. With the decrease of ink viscosity and storage modulus, the formability of printed fiber decreases. For example, the fibers printed with Ink6:4 prepared ink were unable to

support the 3D structure, resulting in the collapse of the printed sample.

5. Applications and discussion

It is well known that the printability of the DIW 3D printing process is ultimately determined by the printed samples' structural integrity and morphological resolution. Based on above systematic study of process parameters, including ink rheological properties, applied pressure, and printing speed, we have completely evaluated the printability of DIW 3D printing.

We found that the Ink8:2 formulation ink can be printed into continuous fibers when the printing speed is 5–70 mm s^{-1} and the applied pressure exceeds a certain threshold, as shown in figure 8(a). Ink accumulation happens as a result of printing speeds less than 5 mm s^{-1} , making it hard to print

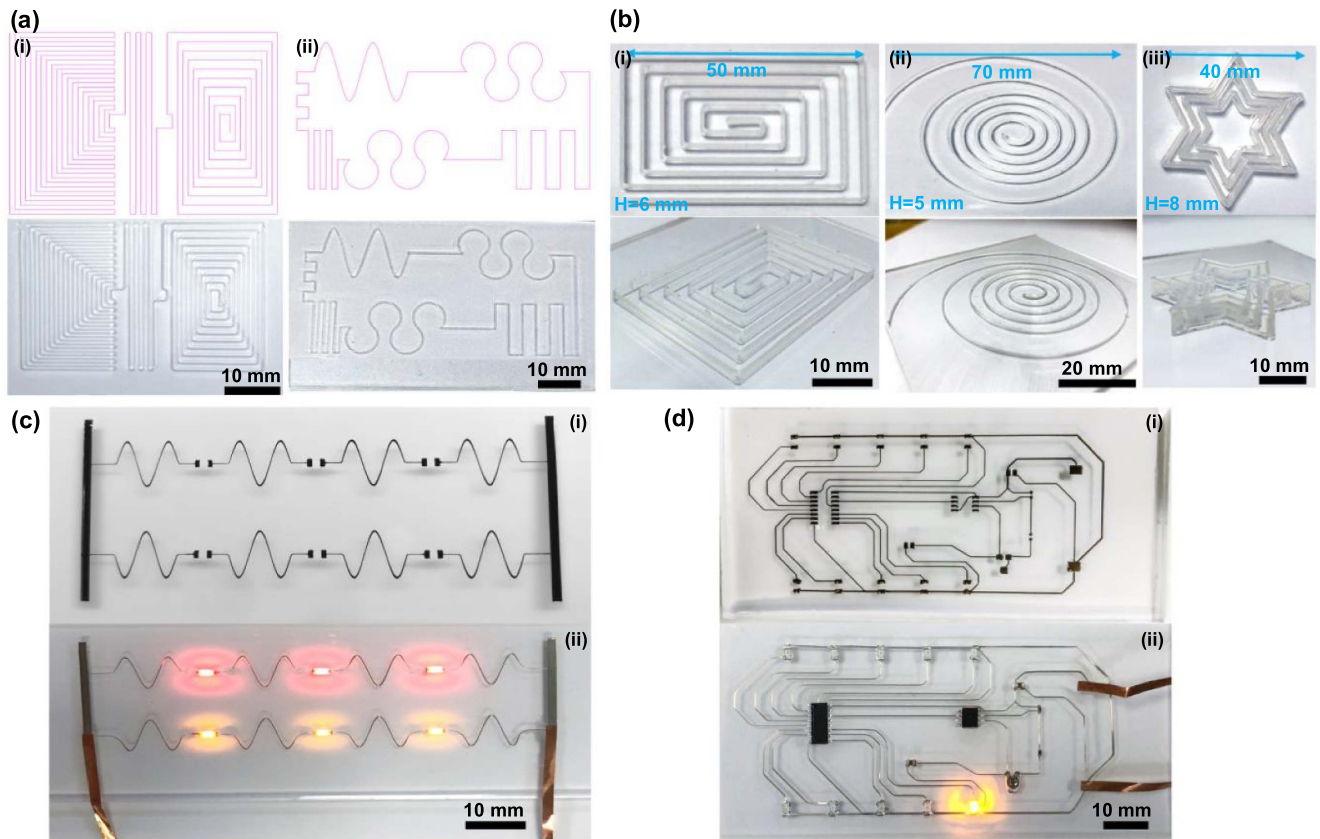


Figure 9. DIW printing application of solid structures under different printing process parameters. (a) 2D patterns printed by PDMS resin inks under different DIW printing processes. The upper figures are CAD models and the lower figures are the corresponding entities. (b) 3D structures, after heat curing, printed by DIW using PDMS resin inks. (c) The DIW printed LED light array device with serpentine lines. (d) Image of an LED circuit fabricated by DIW 3D printing, in which surface mounted electrical components are interconnected with printed silver paste wires on the substrate.

a controllable design pattern. If the printing speed is higher than 70 mm s^{-1} , it is difficult for the printed fibers to deposit onto the substrate due to the high printing speed. And when the applied pressure is less than a certain level, the shear stress is insufficient to drive the flow behavior of the ink, and no ink flows out of the micro nozzle. The right side of figure 8(a) shows the printed fiber profiles corresponding to each printing condition. When the ink concentration is between 50% and 100 wt%, and the applied pressure is higher than a certain level, continuous lines can be printed under the TT110 micro-nozzle, as shown in figure 8(b). The formability of high concentration inks allows 3D models to be printed, while low concentration inks are in droplet form and cannot support the line structures. The applied pressure increases as the ink concentration increases. When the applied pressure is insufficient, unstable flow or even no ink extrusion occurs. The phase diagram predictions can effectively guide experimental print process parameter selections, and the results indicate the validity of the DIW 3D printing process research.

To demonstrate the printability of the process parameters in this study, we printed several samples with the optimized parameters, as displayed in figure 9. Figure 9(a) shows the 2D patterns printed on the acrylic plate using a TT110

micro-nozzle and Ink8:2 PDMS hybrid ink. The printing speed is 20 mm s^{-1} , and the applied pressure is 200 kPa. It is seen that the printed lines demonstrate excellent resolution and smooth contour, which provides a reliable technology for the application of printed circuits. Figure 9(b) shows the as-printed multilayer 3D samples. It can be observed that the 3D structural models remain structurally intact without any collapse. These complete 3D models demonstrate the formability and stable printability of high elasticity modulus hybrid inks.

Additionally, we have prepared flexible LED light arrays based on the DIW 3D printing process study. Curved wires are printed on a flexible substrate to link the LEDs, and these curved leads provide good electrical and mechanical properties. Figure 9(c, i) shows the printed serpentine circuit with good resolution, and the printed wire has a smooth profile. As shown in figure 9(c, ii), the LEDs can be illuminated steadily when the 6 V supply is switched on. To further demonstrate the quality stability of DIW 3D printable circuits, we prepared complex patch circuit systems by DIW 3D printing. Figure 9(d, i) shows the complex patch circuit with good resolution and flatness. We prepared a flat LED flowing light, which includes a CD4017 chip, a control chip, and fifteen SMD (ten LED lights, two $1 \mu\text{F}$ capacitors, and three resistors

with resistance values of 2.2, 10, and 50 k Ω , respectively). Figure 9(d, ii) shows the printed circuits on PDMS substrates with conductive silver paste which was cured at 120 °C for 30 min to obtain complex SMD circuit devices. All LEDs flash continuously when the supply is switched on, proving that the printed circuit can provide a reliable electrical connection.

6. Conclusion

In summary, to facilitate the widespread application of DIW 3D printing technology, we systematically investigated the extrusion mechanism of DIW 3D printing and the influence of process parameters on the quality of printed samples. The range of applicability of different process parameters for the printability of the samples was obtained through the comparative analysis of CFD finite element simulation and DIW printing experiments. The Ink8:2 preparation ink and 110 μm micro-nozzle used in this study enable rapid ($>70 \text{ mm s}^{-1}$), high-resolution, micron scale ($<100 \mu\text{m}$) models. The printability process parameters, including ink rheology, applied pressure, and printing speed, is determined by the resolution and morphological structure of the printed sample. The results show that some exemplary micro-mold geometries were printed using these optimized printable process parameters, and a printed circuit system with reliable electrical connections was successfully demonstrated. Although our demonstration focused on hybrid silicone materials and commercial silver paste, this systematic study towards DIW 3D printing process provides insights into the printing of different inks, thus enabling a wider range of applications for DIW 3D printing technology, such as flexible electronics (i.e. conductive inks), soft robotics (i.e. composite gel inks), biomedical devices (i.e. biocompatible viscous inks) and 4D printing structures (i.e. shape-memory polymers inks, etc.).

Acknowledgments

This work was supported by National Natural Science Foundation of China (Nos. 52188102, U2013213, 51820105008), the Technology Innovation Project of Hubei Province of China under Grant No. 2019AEA171. The project of introducing innovative leading talents in Songshan Lake High-tech Zone, Dongguan City, Guangdong Province (No. 20193421-01RSFJ-G). We also acknowledge the support from Flexible Electronics Research Center of HUST for providing experiment facility.

Conflict of interest

The authors declare that they have no known competing financial interests or personal relationships that could have appeared to influence the work reported in this paper.

ORCID iD

Hao Wu  <https://orcid.org/0000-0003-1494-0848>

References

- [1] Ji Y Y, Luan C C, Yao X H, Fu J Z and He Y 2021 Recent progress in 3D printing of smart structures: classification, challenges, and trends *Adv. Intell. Syst.* **3** 2000271
- [2] Lewis J A 2002 Direct-write assembly of ceramics from colloidal inks *Curr. Opin. Solid State Mater. Sci.* **6** 245–50
- [3] Saadi M A S R, Maguire A, Pottackal N T, Thakur S H, Ikram M M, Hart A J, Ajayan P M and Rahman M M 2022 Direct ink writing: a 3D printing technology for diverse materials *Adv. Mater.* **34** 2108855
- [4] Lewis J A 2006 Direct ink writing of 3D functional materials *Adv. Funct. Mater.* **16** 2193–204
- [5] Ahn B Y, Duoss E B, Motala M J, Guo X Y, Park S-I, Xiong Y J, Yoon J, Nuzzo R G, Rogers J A and Lewis J A 2009 Omnidirectional printing of flexible, stretchable, and spanning silver microelectrodes *Science* **323** 1590–3
- [6] Zhu C, Han T Y J, Duoss E B, Golobic A M, Kuntz J D, Spadaccini C M and Worsley M A 2015 Highly compressible 3D periodic graphene aerogel microlattices *Nat. Commun.* **6** 6962
- [7] Vatani M, Engeberg E D and Choi J W 2015 Conformal direct-print of piezoresistive polymer/nanocomposites for compliant multi-layer tactile sensors *Addit. Manuf.* **7** 73–82
- [8] Shao Y et al 2022 Room-temperature high-precision printing of flexible wireless electronics based on MXene inks *Nat. Commun.* **13** 3223
- [9] Erb R M, Sander J S, Grisch R and Studart A R 2013 Self-shaping composites with programmable bioinspired microstructures *Nat. Commun.* **4** 1712
- [10] Hu W K, Wang Z J, Xiao Y, Zhang S M and Wang J L 2019 Advances in crosslinking strategies of biomedical hydrogels *Biomater. Sci.* **7** 843–55
- [11] Liu X Y, Yuk H, Lin S T, Parada G A, Tang T-C, Tham E, de la Fuente-nunez C, Lu T K and Zhao X H 2018 3D printing of living responsive materials and devices *Adv. Mater.* **30** 1704821
- [12] Wang Z J, Wang Z J, Zheng Y, He Q G, Wang Y and Cai S Q 2020 Three-dimensional printing of functionally graded liquid crystal elastomer *Sci. Adv.* **6** eabc0034
- [13] Kotikian A, McMahan C, Davidson E C, Muhammad J M, Weeks R D, Daraio C and Lewis J A 2019 Untethered soft robotic matter with passive control of shape morphing and propulsion *Sci. Robot.* **4** eaax7044
- [14] Ge Q, Qi H J and Dunn M L 2013 Active materials by four-dimension printing *Appl. Phys. Lett.* **103** 131901
- [15] Ratna D and Karger-Kocsis J 2008 Recent advances in shape memory polymers and composites: a review *J. Mater. Sci.* **43** 254–69
- [16] Hou Z Z, Lu H, Li Y, Yang L X and Gao Y 2021 Direct ink writing of materials for electronics-related applications: a mini review *Front. Mater.* **8** 647229
- [17] Wei P R, Leng H M, Chen Q Y, Advincula R C and Pentzer E B 2019 Reprocessable 3D-printed conductive elastomeric composite foams for strain and gas sensing *ACS Appl. Polym. Mater.* **1** 885–92
- [18] Huang X et al 2022 Flexible mechanical metamaterials enabled electronic skin for real-time detection of unstable grasping in robotic manipulation *Adv. Funct. Mater.* **32** 2109109
- [19] Skylar-Scott M A, Uzel S G M, Nam L L, Ahrens J H, Truby R L, Damaraju S and Lewis J A 2019 Biomanufacturing of organ-specific tissues with high cellular density and embedded vascular channels *Sci. Adv.* **5** eaaw2459
- [20] Jakus A E, Secor E B, Rutz A L, Jordan S W, Hersam M C and Shah R N 2015 Three-dimensional printing of high-content graphene scaffolds for electronic and biomedical applications *ACS Nano* **9** 4636–48

- [21] Schaffner M, Faber J A, Pianegonda L, Rühls P A, Coulter F and Studart A R 2018 3D printing of robotic soft actuators with programmable bioinspired architectures *Nat. Commun.* **9** 878
- [22] Skylar-Scott M A, Mueller J, Visser C W and Lewis J A 2019 Voxellated soft matter via multimaterial multinozzle 3D printing *Nature* **575** 330–5
- [23] Wan X, Luo L, Liu Y J and Leng J S 2020 Direct ink writing based 4D printing of materials and their applications *Adv. Sci.* **7** 2001000
- [24] Lewis J A, Smay J E, Stuecker J and Cesarano J III 2006 Direct ink writing of three-dimensional ceramic structures *J. Am. Ceram. Soc.* **89** 3599–609
- [25] Neumann T V and Dickey M D 2020 Liquid metal direct write and 3D printing: a review *Adv. Mater. Technol.* **5** 2000070
- [26] Forzatti P, Ballardini D and Sighicelli L 1998 Preparation and characterization of extruded monolithic ceramic catalysts *Catal. Today* **41** 87–94
- [27] Wang J F, Liu Y Y, Fan Z M, Wang W, Wang B and Guo Z H 2019 Ink-based 3D printing technologies for graphene-based materials: a review *Adv. Compos. Hybrid Mater.* **2** 1–33
- [28] Ji H H, Zhao J, Chen J, Shimai S Z, Zhang J, Liu Y, Liu D Z and Wang S W 2022 A novel experimental approach to quantitatively evaluate the printability of inks in 3D printing using two criteria *Addit. Manuf.* **55** 102846
- [29] Nesaei S, Rock M, Wang Y, Kessler M R and Gozen A 2017 Additive manufacturing with conductive, viscoelastic polymer composites: direct-ink-writing of electrolytic and anodic poly (ethylene oxide) composites *J. Manuf. Sci. Eng.* **139** 111004
- [30] Hausmann M K, Rühls P A, Siqueira G, Läger J, Libanori R, Zimmermann T and Studart A R 2018 Dynamics of cellulose nanocrystal alignment during 3D printing *ACS Nano* **12** 6926–37
- [31] Bruneaux J, Therriault D and Heuzey M-C 2008 Micro-extrusion of organic inks for direct-write assembly *J. Micromech. Microeng.* **18** 115020
- [32] Yuk H and Zhao X H 2018 A new 3D printing strategy by harnessing deformation, instability, and fracture of viscoelastic inks *Adv. Mater.* **30** 1704028
- [33] Fang H, Wang L, Fu Z Z, Xu L, Guo W, Huang J, Wang Z L and Wu H 2023 Anatomically designed triboelectric wristbands with adaptive accelerated learning for human-machine interfaces *Adv. Sci.* **10** 2205960
- [34] Yang G G et al 2022 Adhesive and hydrophobic bilayer hydrogel enabled on-skin biosensors for high-fidelity classification of human emotion *Adv. Funct. Mater.* **32** 2200457
- [35] Herschel W H and Bulkley R 1926 Konsistenzmessungen von gummi-benzollösungen *Kolloid-Z.* **39** 291–300
- [36] Deng P, Zhang J, Liu F H, Liu K J, Liu H and Zhang L 2013 Shear-induced flow behavior of three polymers in different size dies *J. Macromol. Sci. B* **52** 651–61
- [37] Wilms P, Wieringa J, Blijdenstein T, Van Malssen K, Hinrichs J and Kohlus R 2022 On the difficulty of determining the apparent wall slip of highly concentrated suspensions in pressure driven flows: the accuracy of indirect methods and best practice *J. Non-Newton. Fluid Mech.* **299** 104694
- [38] Estelle K T and Gozen B A 2022 Complex ink flow mechanisms in micro-direct-ink-writing and their implications on flow rate control *Addit. Manuf.* **59** 103183
- [39] Del-Mazo-Barbara L and Ginebra M-P 2021 Rheological characterisation of ceramic inks for 3D direct ink writing: a review *J. Eur. Ceram. Soc.* **41** 18–33
- [40] Tubío C R, Antelo J, Guitián F and Gil A 2018 3D printed composites of copper-aluminum oxides *3D Print. Addit. Manuf.* **5** 46–52
- [41] Ozbolat V, Dey M, Ayan B, Povilanskas A, Demirel M C and Ozbolat I T 2018 3D printing of PDMS improves its mechanical and cell adhesion properties *ACS Biomater. Sci. Eng.* **4** 682–93
- [42] Wehner M, Truby R L, Fitzgerald D J, Mosadegh B, Whitesides G M, Lewis J A and Wood R J 2016 An integrated design and fabrication strategy for entirely soft, autonomous robots *Nature* **536** 451–5
- [43] Nachbaur L, Mutin J C, Nonat A and Choplin L 2001 Dynamic mode rheology of cement and tricalcium silicate pastes from mixing to setting *Cem. Concr. Res.* **31** 183–92
- [44] White F M 2009 Fluid mechanics *Viscous Flow in Ducts* ed F M White (New York: E-Publishing Inc.) pp 347–59
- [45] Jiang Z, Ouyang T, Yao X D and Fei Y Q 2016 Die swell behavior of liquid crystalline mesophase pitch *J. Mater. Sci.* **51** 7361–9